# *Decreased monsoon precipitation in the Northern Hemisphere due to anthropogenic aerosols*

Article

Supplemental Material

# Auxilary material for:
# Decreased monsoon precipitation in the Northern Hemisphere due to anthropogenic aerosols

## Geophysical Research Letters

*D. Polson, M. Bollasina, G. C. Hegerl and L. J. Wilcox*

### *a. 2-signal detection and attribution results*

Figure S1 shows the results of a 2-signal detection and attribution analysis for combinations of anthropogenic aerosol and natural forcings (AA&NAT) and greenhouse gas and natural forcing (GHG&NAT) as described in the main the paper.

### *b. Spatial precipitation patterns in NHSM region*

Figure S2 shows spatial linear trend patterns for MJJAS precipitation for observations (GPCC) and the multi-model mean for each individual forcing. The spatial pattern of ALL and ANT are more consistent with the AA than the GHG multi-model mean. GHG multi-model mean shows increasing precipitation over most of the NHSM region, while the AA multi-model means shows mostly drying trends. The observed trends show an increase in precipitation over the whole period over South America and parts of Asia, while the ALL multi-model mean shows a decrease in precipitation in these regions. Conversely, in parts of Africa, the ALL multi-model mean has increasing precipitation while the observations show an overall decrease, though the models do not tend to show much consistency in the sign of the trends (less than 2/3 of simulations have trends of the same sign). However the timeseries for the observed mean precipitation in the NHSM region (Figs S3-S6) show that precipitation

decreases from 1951, reaches a minimum in the mid-1980s and then begins to recover, with the observed recovery greater in Asia than Africa, a behaviour not well captured by a linear trend. While ALL seems to capture the general decrease in precipitation from the 1950s to 1980s, during the 1990s, it tends to underestimate the recovery over Asia and overestimate the recovery over Africa.

The role of the indirect aerosol effect is investigated by plotting the multi-model mean trends and timeseries for the ALL forced models that included both the indirect and direct effects and the models that include the direct effect only (Figs. S2 and S3). The mean precipitation change for the whole region is largely the same for both ensembles. However the spatial trend patterns show interesting differences, particularly over Asia. The models that include the indirect effect tend to simulate drier conditions over India and central China than the models that include the direct effect only. These results suggest that the relative influence of the indirect and direct effects on precipitation in the models varies between regions.

The spatial trend patterns are also plotted for 1951-1985 and 1985-2005 (Figure S7 and S8). The spatial trend pattern for 1951-1985 is similar for the ALL forced multi-model mean and observations, with both showing largely decreasing precipitation from the 1950s to mid-1980s. The ANT and AA multi-model means also show a similar pattern, suggesting that aerosols are at least in part responsible for this decrease. However the increase in precipitation in Africa from 1985-2005 is overestimated by the ALL forced multi-model, while the pattern of increasing precipitation over East Asia and decreasing precipitation over India is not reproduced by the ALL forced multi-model mean, though the AA forced multi-model mean does gives a similar pattern. There is, however, little consistency between ALL forced simulations on the sign of the trends from 1985-2005.

To highlight the variability between simulated trends from 1951-2005, we calculate an error score, $Sk$, for each individual model simulation compared to observations using

$$Sk = rmse + N_{err} \quad (1)$$

where $rmse$ is root mean square error of simulated trends with respect to the observations and $N_{err}$ is the number of grid boxes where the sign of the trend disagrees with observations. Both $rmse$ and $N_{err}$ are calculated as a fraction of the mean of values for all simulations. Figures S9 and S10 show the 1951-2005 trends for the 6 simulations with the most and least agreement with the observations. Note this is not an assessment of model performance, rather the aim is to demonstrate the variability of the trend patterns between simulations, hence we use individual model simulations, not model ensembles. No single simulation perfectly reproduces the observed trends in all regions (shown in Figure S2), however the observed increase/decrease in precipitation in each region is simulated by more than one of the 'best' simulations. The 'worst' simulations all fail to fully reproduce the decrease in precipitation over Africa, but do tend to capture the drying trends over east Asia. The multi-model mean trends for an ensemble of ALL forced models that uses only one simulation per modelling group (as opposed to all simulations available used in the main results), shows that the trend patterns do not appear to be biased to any one model or modelling centre (not shown).

*c. Sensitivity of detection and attribution results*

The inconsistency in the observed and model spatial trend patterns over the period 1951-2005 does not seem to affect the detection and attribution results for the mean temporal signal for the whole region. This may be due to a coincidental cancellation of the positive and negative changes in different regions. However, it is more likely that while the models capture most of the temporal variation over this period, the recent increase in precipitation over many regions is not captured correctly by the models. This may be because the observed changes are simply due to internal climate variability, because the forcings in the models are not consistent with reality, because of uncertainty in the observations or a combination

of these factors. To check the sensitivity of the results to the exclusion of different regions, the analysis was also repeated excluding first South America (supplementary Figure S11(a)), then Africa (supplementary Figure S11(b)) and finally Asia (supplementary Figure S11(c)). In each case the results are broadly similar to those for the whole region. The analysis was also repeated to verify whether the results were sensitive to the inclusion of the mid-latitude NHSM region. The 3-signal analysis shows similar detection of AA forcing when the mid-latitudes NHSM regions are included (Figure S11(d)).

The detection and attribution analysis was also repeated using the same model ensemble for each pair of forcings in the 2-signal analysis (Figs. S12(a)-(d)) and for the GHG, NAT and AA forcing in the 3-signal analysis (Figure S12(e)). The detection results for different forcings are identical to the results using all available models and are therefore not sensitive to the model ensemble (see *Zhang et al.* (2007)).

# Linearity of the individual forcings

In the above the analysis, we assumed that the combined influence of all external forcings can be well approximated by a linear combination of individual forcings, and that by adding the contribution of GHG, AA and NAT, we can reproduce the changes in precipitation from the ALL forced simulations (i.e. ignoring the influence of other forcings such as land use change). To check if this is a reasonable assumption we compare the ALL multi-model mean to the sum of GHG, NAT and AA multi-model means (Figure S13(a)), using the method described in Schurer et al. (*Schurer et al.* 2014). Subtracting the sum of GHG+NAT+AA from ALL, gives the residual shown in Figure S13(b). If the forcings add linearly, then the residual and the internal variability should be consistent. The internal variability is calculated from the samples of noise derived from the ALL forcing ensemble as described in the methods section. The standard deviation is calculated for each member of the noise ensemble and as model simulations have different internal variability, we use the mean standard deviation

for the whole ensemble to check the consistency of the residual with internal variability. If the residual is within 2 standard deviations of the internal variability, then we can say that the assumption of linearity has not been disproven. The results show that the assumption of linearity has not been violated.

*d. Observational versus model variability*

To check that the variability in the models is consistent with the observed variability, the variance for MMJAS precipitation was calculated for South America, Africa and Asia, for each observational dataset and every simulation in the ALL ensemble. Figure S14 shows the range of the ratio of the variance between the observational datasets and each individual model simulation. The results for both the unsmoothed and 9-year smoothed precipitation, show that the models tend to underestimate the variance in the observations, though in most cases a variance ratio of 1 is within the 90% confidence interval. Only for Africa, for the 9-year smoothed data, does the 90% confidence interval exceed 1. However doubling the model variance, as done when calculating the noise samples for the detection and attribution analysis, gives a variance ratio of 1 within the 90% confidence interval. Note that the detection and attribution results remain valid if the African monsoon region is excluded (Figure S11).

# REFERENCES

Schurer, A. P., S. F. B. Tett, and G. C. Hegerl (2014), Small influence of solar variability on climate over the past millennium, *Nature Geosci*, *7*, 104–108.

120 Taylor, K. E., R. J. Stouffer, and G. A. Meehl (2011), An Overview of CMIP5 and the
121 Experiment Design, *Bull. Amer. Meteor. Soc.*, *93*, 485–498.

122 Zhang, X., et al. (2007), Detection of human influence on twentieth-century precipitation
123 trends, *Nature*, *448*(7152), 461–465.

# List of Tables

TABLE 1. List of models and numbers of simulations used in this analysis (*Taylor et al.* 2011).

| *InstituteID* | *ModelName* | *ALL* | *ANT* | *GHG* | *AA* | *NAT* | *IND + DIR* | *DIR* |
|---|---|---|---|---|---|---|---|---|
| BCC | BCC-CSM1.1 | 4 | | | | 1 | | 4 |
| CCCMA | CanESM2 | 5 | | 5 | 4 | 5 | 5 | |
| CMCC | CMCC-CESM | 1 | | | | | 1 | |
| CMCC | CMCC-CMS | 1 | | | | | 1 | |
| CMCC | CMCC-CM | 1 | | | | | 1 | |
| CNRM-CERFACS | CNRM-CM5 | 5 | | 5 | | 5 | 5 | |
| EC-EARTH | EC-EARTH | 4 | | | | | | |
| FIO | FIO-ESM | 1 | | | | | | |
| NASA GISS | GISS-E2-H | 5 | 4 | 5 | 1 | 5 | 5 | |
| NASA GISS | GISS-E2-H-CC | 1 | | | | | 1 | |
| NASA GISS | GISS-E2-R | 5 | 2 | 5 | 1 | 5 | 5 | |
| MOHC | HadGEM2-ES | 4 | | 4 | | 4 | 4 | |
| MOHC | HadGEM2-CC | 1 | | | | | 1 | |
| MOHC | HadCM3 | 5 | | | | | 5 | |
| INM | INM-CM4 | 2 | | | | | | |
| IPSL | IPSL-CM5A-LR | 4 | 3 | 5 | | 1 | 4 | |
| IPSL | IPSL-CM5A-MR | 1 | | 3 | | 3 | 1 | |
| NCC | NorESM1-M | 3 | | 1 | 1 | 1 | 3 | |
| NCC | NorESM1-ME | 1 | | | | | 1 | |
| CSIRO-QCCCE | CSIRO-Mk3.6.0 | 5 | 5 | 5 | 5 | 5 | 5 | |
| CSIRO-BOM | ACCESS1.0 | 1 | | | | | 1 | |
| NOAA GFDL | GDFL-ESM2G | 5 | | | | | | 5 |
| NOAA GFDL | GDFL-ESM2M | 2 | 1 | | | 1 | | 2 |
| NOAA GFDL | GFDL-CM3 | 5 | 3 | 3 | 3 | 3 | 5 | |
| MIROC | MIROC5 | 3 | | | | | 3 | |
| MIROC | MIROC-ESM | 3 | | 1 | | 1 | 3 | |
| MIROC | MIROC-ESM-CHEM | 1 | | 1 | | 1 | 1 | |
| MPI-M | MPI-ESM-LR | 3 | | | | | | 3 |
| MRI | MRI-CGCM3 | 5 | | 1 | | 1 | 5 | |
| NCAR | CCSM4 | 5 | | 3 | | 3 | | 5 |
| NSF-DOE-NCAR | CESM1(BGC) | 2 | | | | | | 2 |
| NSF-DOE-NCAR | CESM1(CAM5) | 3 | | | | | 3 | |
| NSF-DOE-NCAR | CESM1(CAM5.1,FV2) | 4 | | 2 | | 2 | 4 | |
| NSF-DOE-NCAR | CESM1(FASTCHEM) | 3 | | | | | 3 | |
| NSF-DOE-NCAR | CESM1(WACCM) | 1 | | | | | | 1 |

# List of Figures

S11 Detection and attribution results for observed changes in NHSM precipitation testing for overweighting of individual regions. Shown are the 3-signal analysis results for greenhouse gas (GHG), natural (NAT) and anthropogenic aerosol (AA) forcing for the NHSM region (a)-(c), excluding South American, African and Asian monsoon regions and (d), including the mid-latitude regions. Results are shown for four observational datasets, CRU (CRU), Zhang (ZHA), VasClimO (VAS) and GPCC (GPCC). Crosses show the best-guess scaling factor for the multi-model mean, thick lines are the 90% confidence interval based on the raw variance and thin lines are the 90% confidence intervals when model variance has been doubled. The residual consistency test is passed for all cases. Stars (*) show where forcing is detected and two stars show where forcing is detected but inconsistent with a scaling factor of 1. 24

S12 Detection and attribution results for observed changes in NHSM precipitation where the same models are used to produce the fingerprint for each combination of forcings. (a)-(d), 2-signal and (e), 3-signal detection and attribution analysis. (a), anthropogenic (ANT) and natural (NAT) forcing, (b), anthropogenic aerosol (AA) and natural (NAT) forcing, (c), anthropogenic aerosol (AA) and greenhouse gas (GHG) forcing, (d), greenhouse gas (GHG) and natural (NAT) forcing and (e), greenhouse gas (GHG), natural (NAT) and anthropogenic aerosol (AA) forcing. Results are shown for four observational datasets, CRU (CRU), Zhang (ZHA), VasClimO (VAS) and GPCC (GPCC). Crosses show the best-guess scaling factor for the multi-model mean, thick lines are the 90% confidence interval based on the raw variance and thin lines are the 90% confidence intervals when model variance has been doubled. The residual consistency test is passed for all cases. Stars (*) show where forcing is detected and two stars show where forcing is detected but inconsistent with a scaling factor of 1. 25

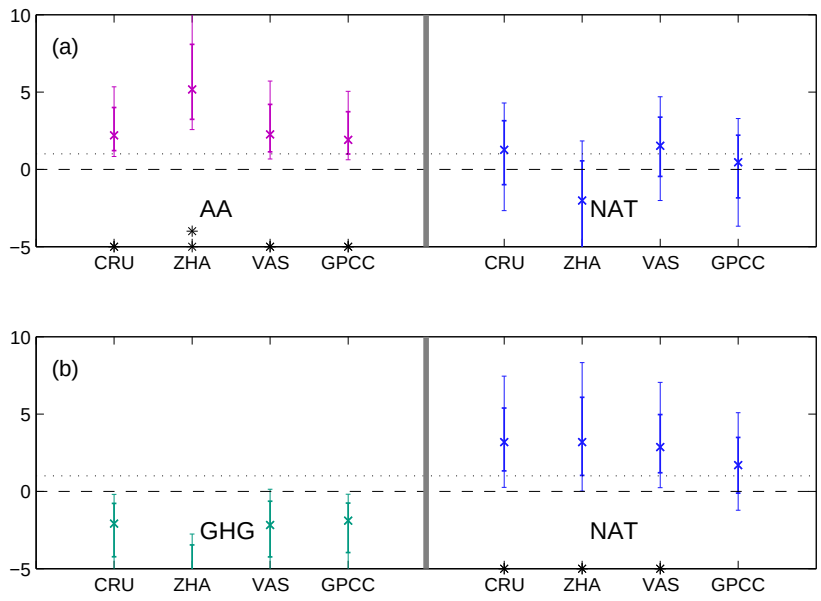


FIG. S1. Detection and attribution results for observed changes in Northern Hemisphere Summer monsoon precipitation. (a), 2-signal regression for anthropogenic aerosol (AA) and natural (NAT) forcing. (b), 2-signal regression for greenhouse gas (GHG), and natural (NAT) forcing. Results are shown for four observational datasets, CRU (CRU), Zhang (ZHA), VasClimO (VAS) and GPCC (GPCC). Crosses show the best-guess scaling factor for the multi-model mean, thick lines are the 90% confidence interval based on the raw variance and thin lines are the 90% confidence intervals when model variance has been doubled. The residual consistency test is passed for all cases. Stars (*) show where forcing is detected and two stars show where forcing is detected but inconsistent with a scaling factor of 1.

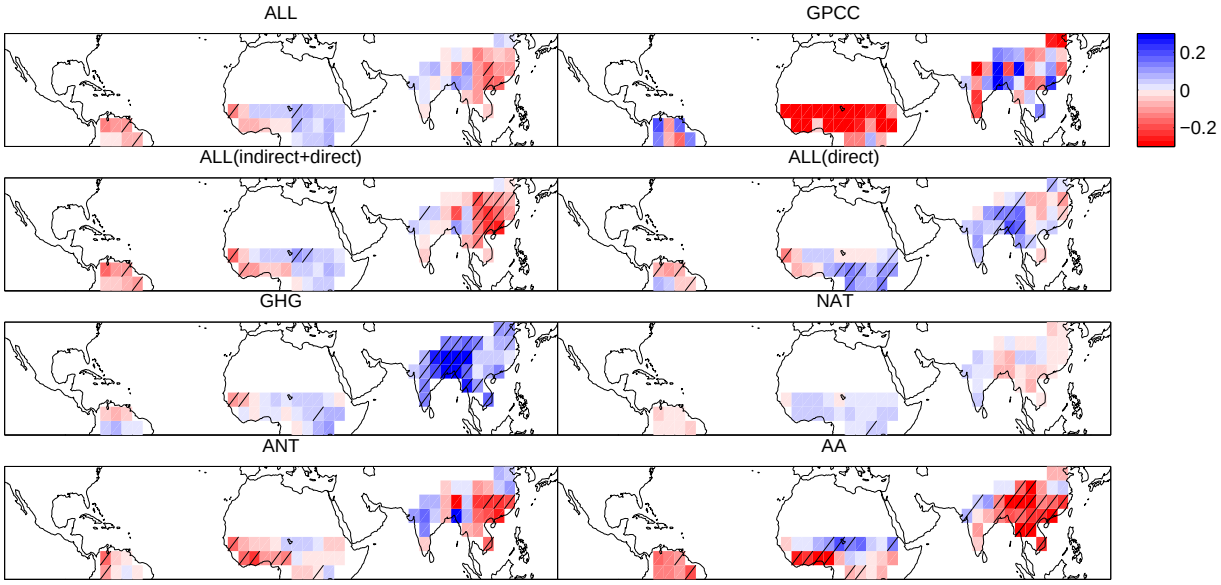


FIG. S2. Observed and multi-model mean model MJJAS precipitation linear trends (mm/month/year) for 1951-2005. Shown are for all external forcings (ALL), observed (GPCC), all forced models that include both the indirect and direct effects (ALL(indirect+direct)), all forced models that only include the direct effect (ALL(direct)), greenhouse gas forcing (GHG), natural forcings (NAT), anthropogenic forcings (ANT) and anthropogenic aerosol forcing (AA). Hatching shows were over 2/3 of individual simulations produce trends of the same sign. Information on whether the indirect effect is included was not available for all models so the combined ensemble of ALL(indirect+direct) + ALL(direct) is less than ALL, explaining any inconsistencies in the hatching.

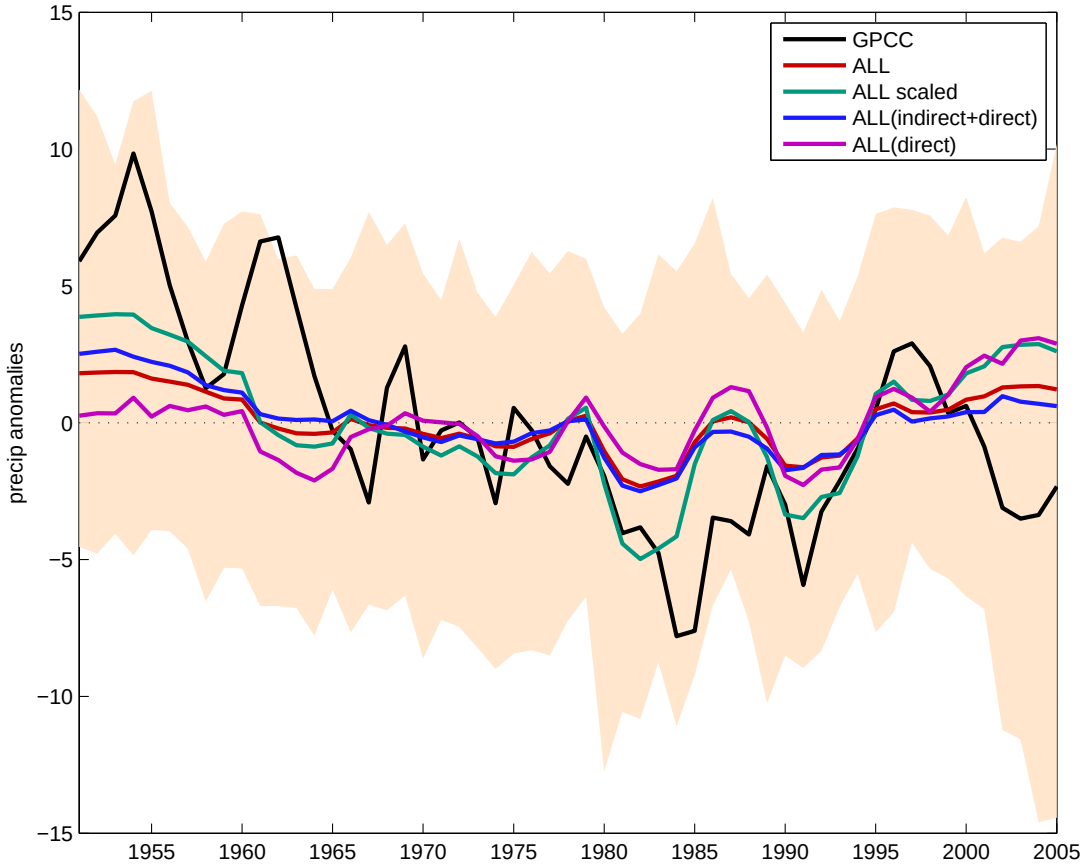


FIG. S3. As Figure 1 but for ALL(indirect+direct) and ALL(direct) ensembles. Shown are the timeseries for the GPCC observational dataset and the multi-model mean for all external forcings (ALL), the all external forcing scaled by the GPCC total least squares scaling factor (ALL scaled), the multi-model mean all forced models that include the indirect and direct effects (ALL(indirect+direct)) and models that include the direct effect only (ALL(direct)). Orange shading shows the 5%-95% range for the ALL ensemble. Models are masked to the GPCC dataset.

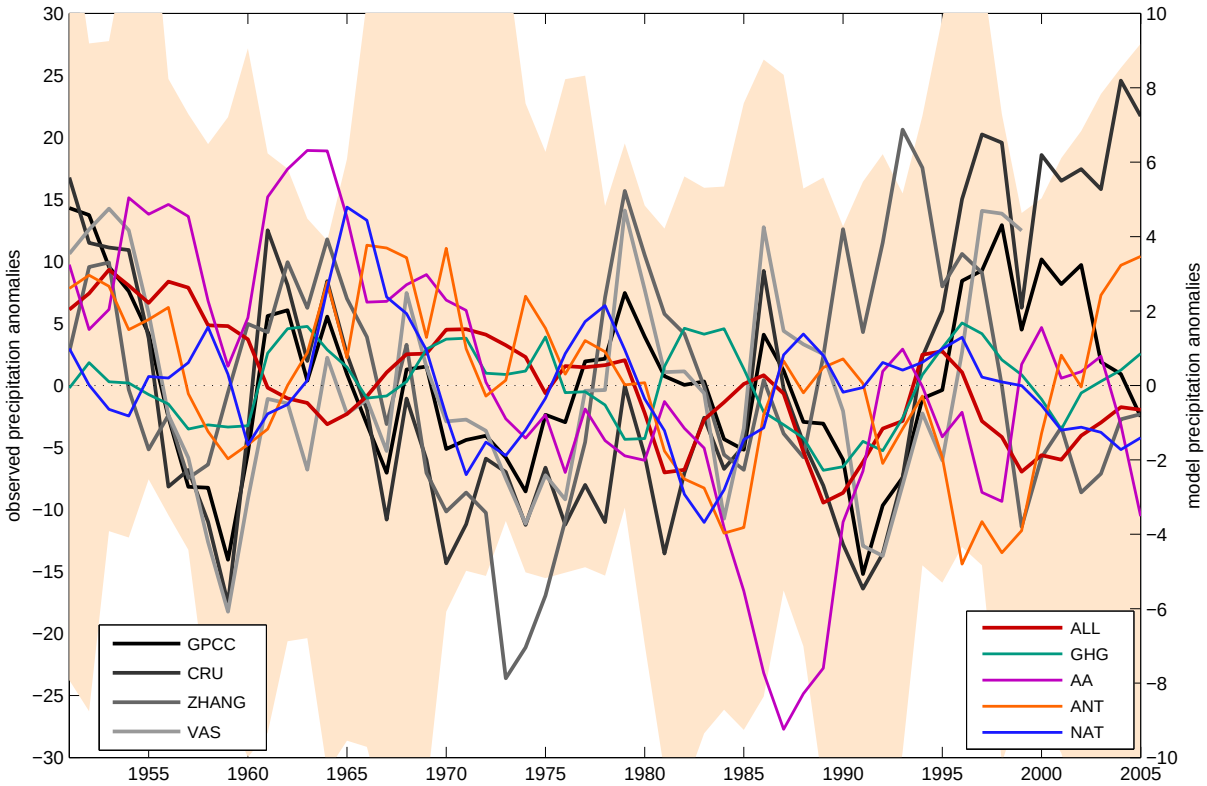


FIG. S4. As Figure 1 for the South American NHSM region. Shown are for 4 observations datasets, CRU, Zhang, VasClimO and GPCC and multi-model mean for all external forcings (ALL), greenhouse gas forcing (GHG), anthropogenic aerosol forcing (AA), natural forcing (NAT) and anthropogenic forcings (ANT). Note multi-model means are plotted on a different scale to observations. Orange shading shows the 5%-95% range for the ALL ensemble, plotted on the same scale as observations. Models are masked to the GPCC dataset.

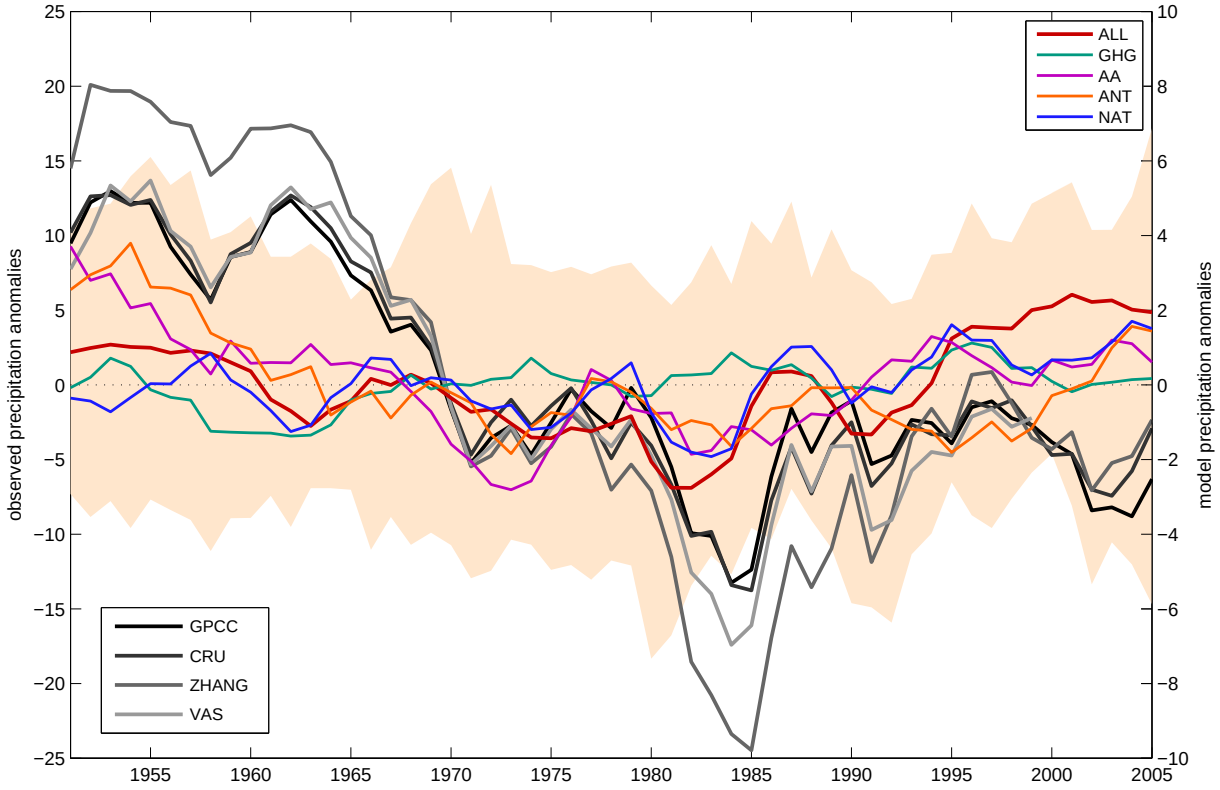


FIG. S5. As Figure 1 for the African NHSM region. Shown are 4 observations datasets, CRU, Zhang, VasClimO and GPCC and multi-model mean for all external forcings (ALL), greenhouse gas only forcing (GHG), anthropogenic aerosol only forcing (AA), natural only forcing (NAT) and anthropogenic forcings (ANT). Note multi-model means are plotted on a different scale to observations. Orange shading shows the 5%-95% range for the ALL ensemble, plotted on the same scale as observations. Models are masked to the GPCC dataset.

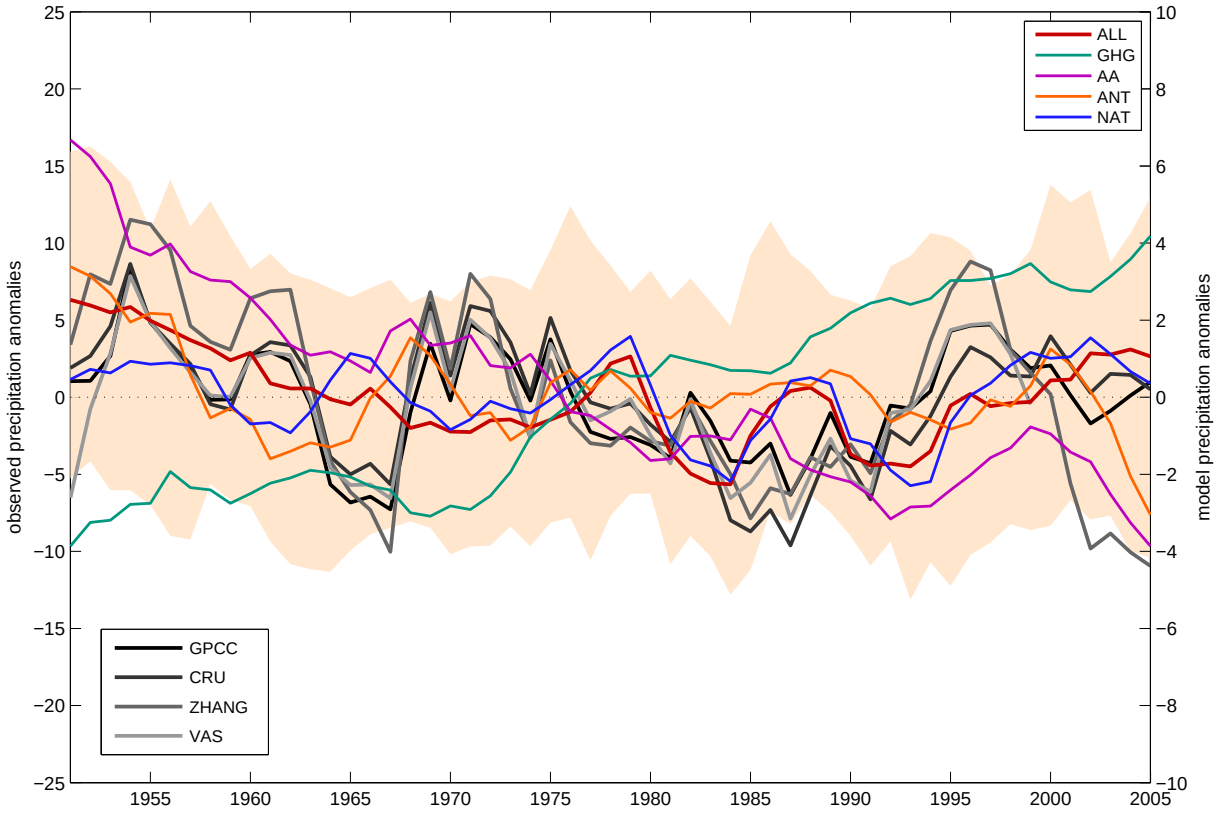


FIG. S6. As Figure 1 for the Asian NHSM region. Shown are 4 observations datasets, CRU, Zhang, VasClimO and GPCC and multi-model mean for all external forcings (ALL), greenhouse gas only forcing (GHG), anthropogenic aerosol only forcing (AA), natural only forcing (NAT) and anthropogenic forcings (ANT). Note multi-model means are plotted on a different scale to observations. Orange shading shows the 5%-95% range for the ALL ensemble, plotted on the same scale as observations. Models are masked to the GPCC dataset.

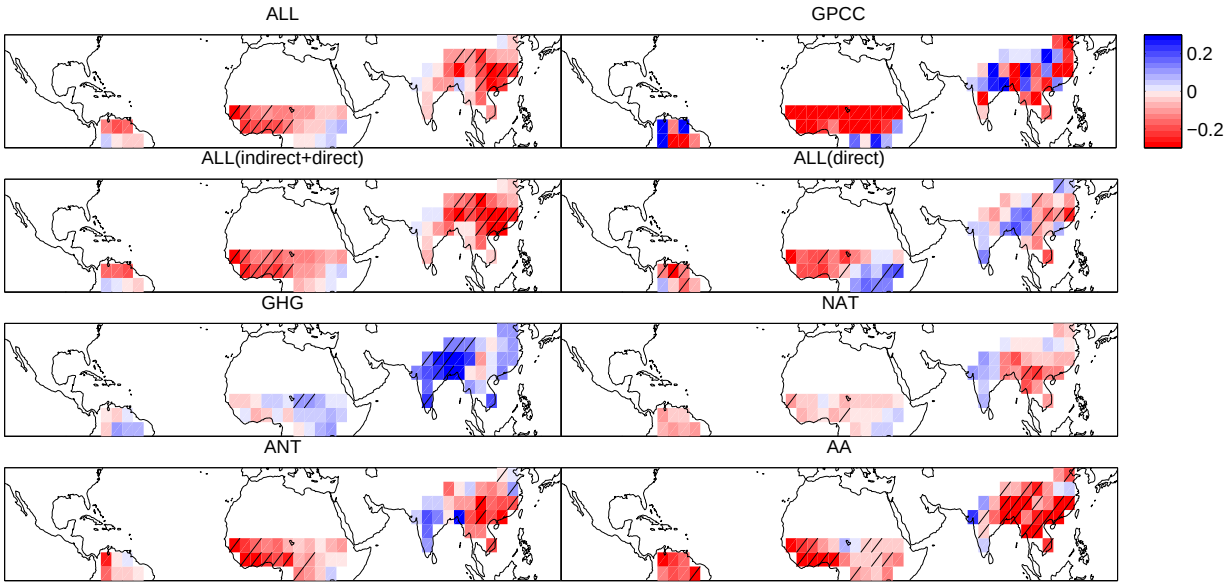


FIG. S7. Figure S2 except precipitation linear trends (mm/day/year) are for 1951-1985.

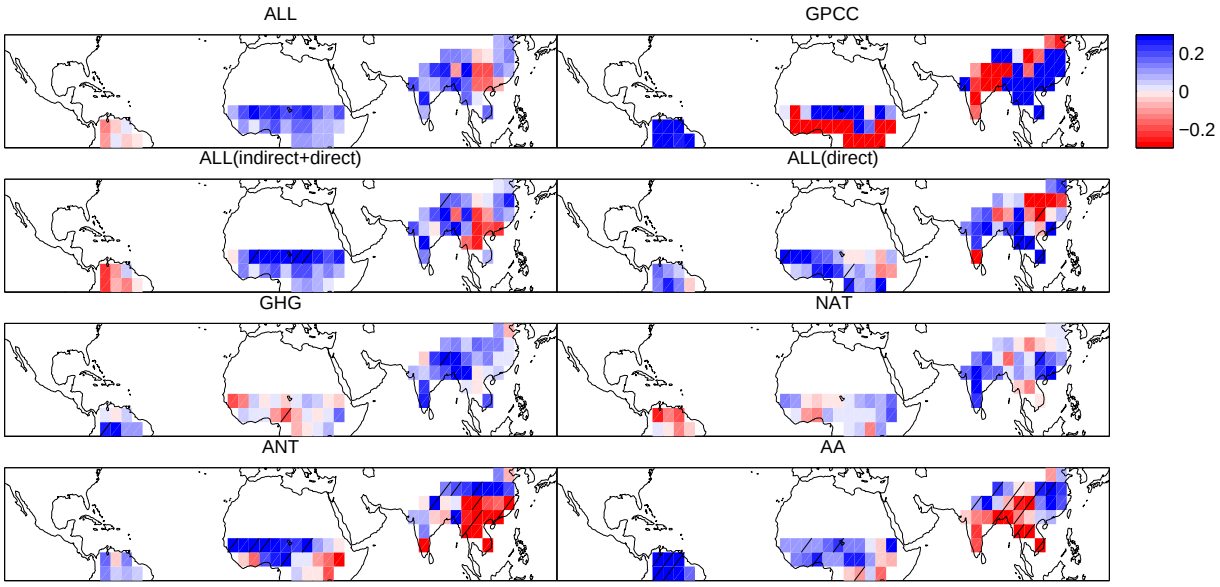


FIG. S8. As Figure S2 except precipitation linear trends (mm/day/year) are for 1985-2005.

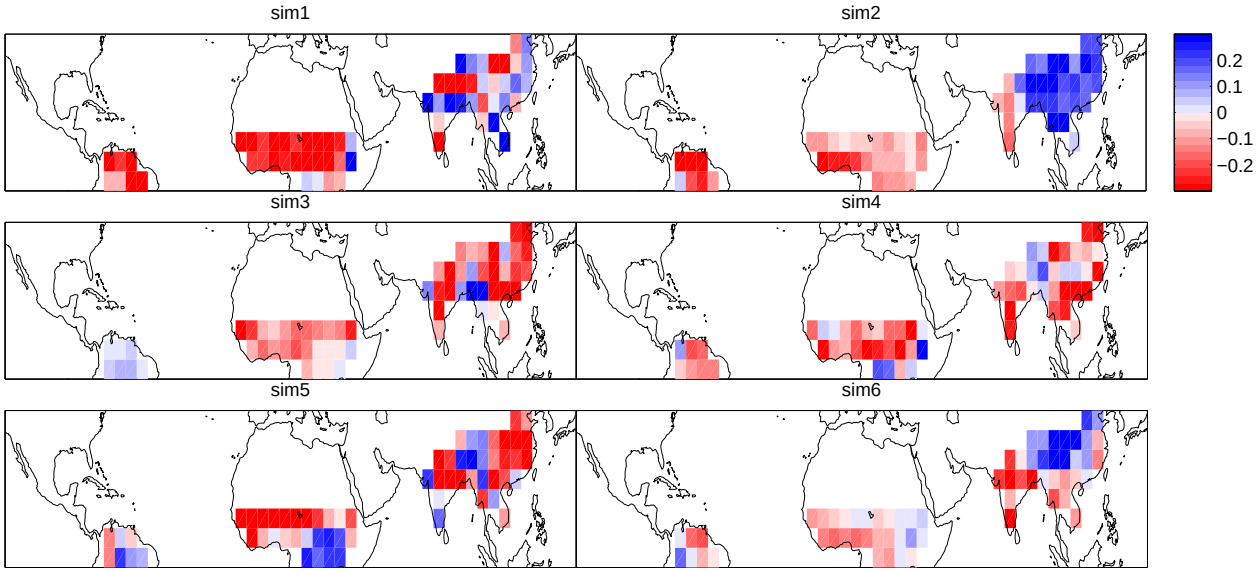


FIG. S9. Linear trends for simulations that best agree with observations. ALL forced simulation MJJAS precipitation linear trends (mm/day/year) for 1951-2005 for the 6 simulations that best agree with observations (lowest error score).

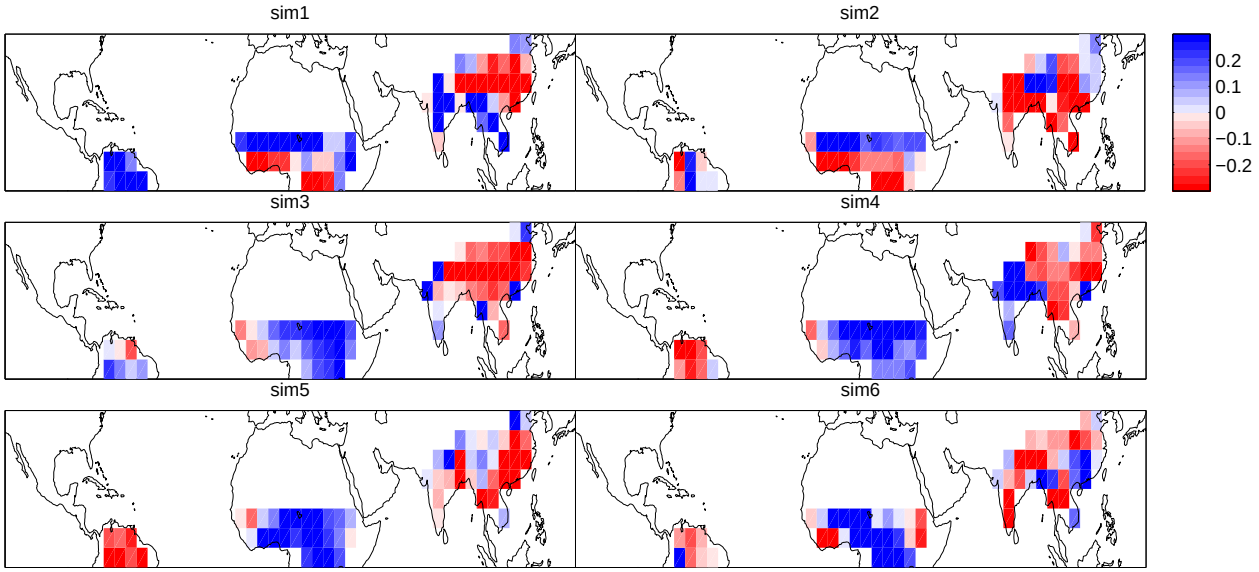


FIG. S10. Linear trends for simulations with least agreement with observations. ALL forced simulation MJJAS precipitation linear trends (mm/day/year) for 1951-2005 for 6 simulations with least agreement with observations (highest error score).

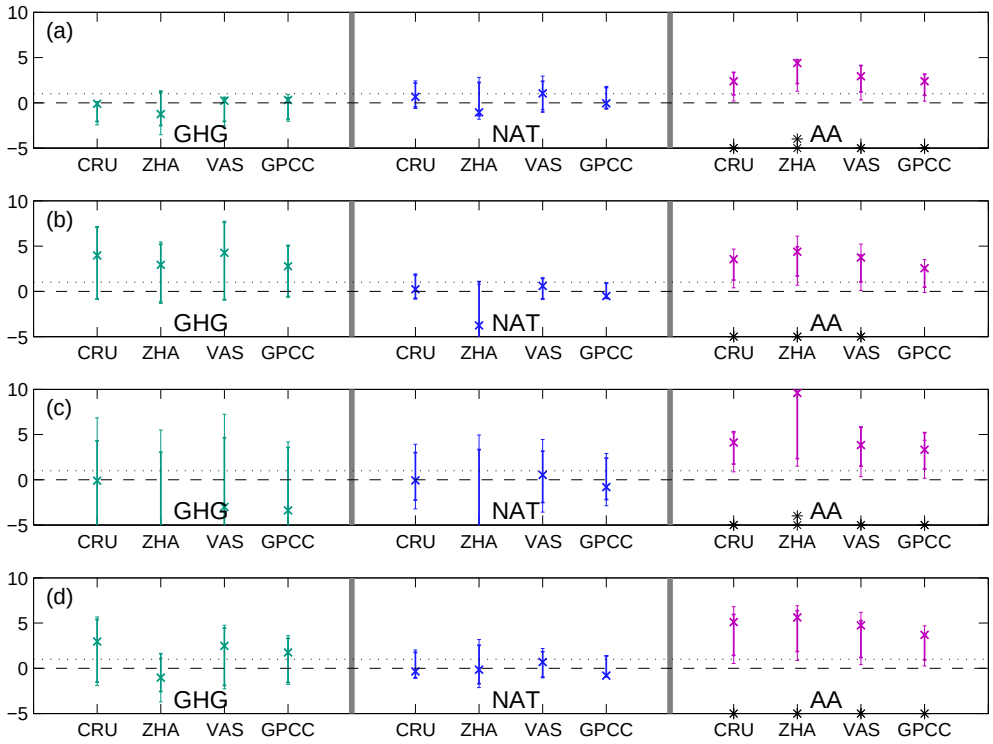


FIG. S11. Detection and attribution results for observed changes in NHSM precipitation testing for overweighting of individual regions. Shown are the 3-signal analysis results for greenhouse gas (GHG), natural (NAT) and anthropogenic aerosol (AA) forcing for the NHSM region (a)-(c), excluding South American, African and Asian monsoon regions and (d), including the mid-latitude regions. Results are shown for four observational datasets, CRU (CRU), Zhang (ZHA), VasClimO (VAS) and GPCC (GPCC). Crosses show the best-guess scaling factor for the multi-model mean, thick lines are the 90% confidence interval based on the raw variance and thin lines are the 90% confidence intervals when model variance has been doubled. The residual consistency test is passed for all cases. Stars (*) show where forcing is detected and two stars show where forcing is detected but inconsistent with a scaling factor of 1.

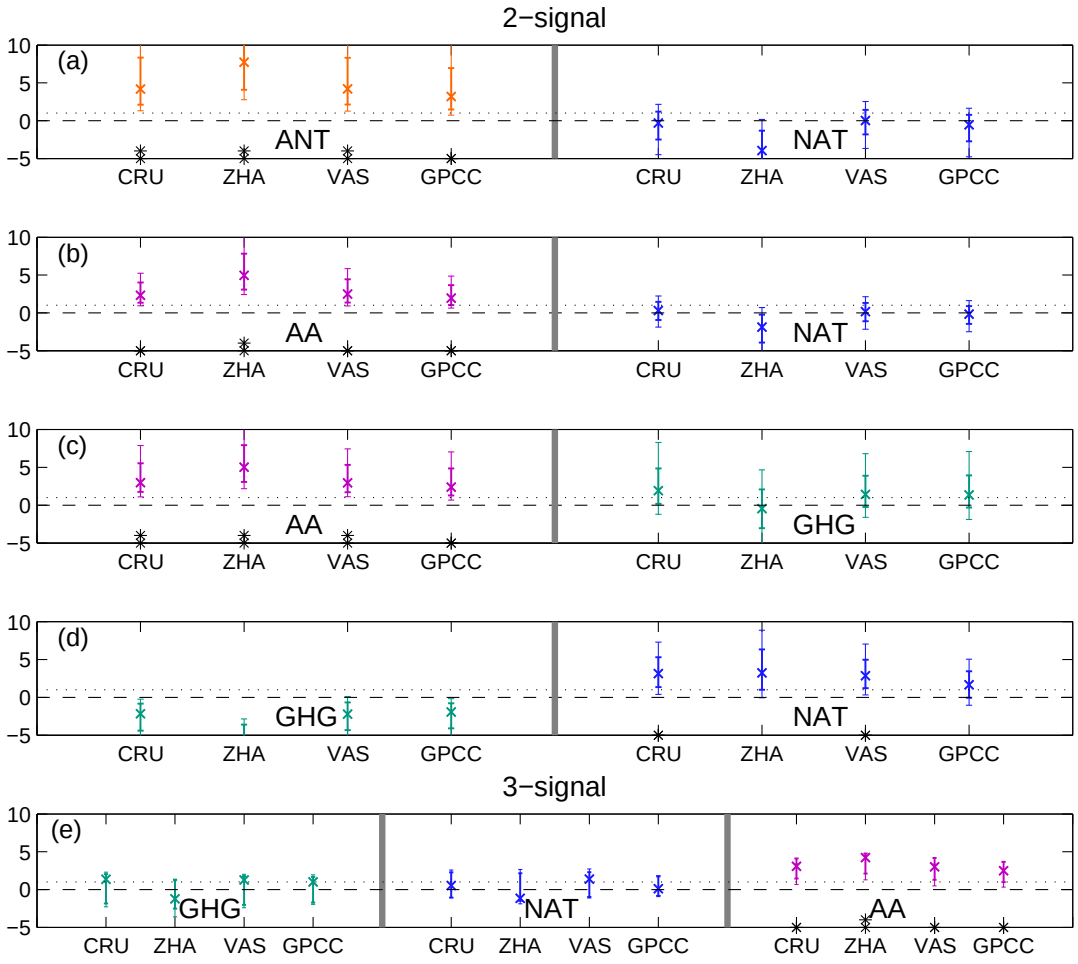


FIG. S12. Detection and attribution results for observed changes in NHSM precipitation where the same models are used to produce the fingerprint for each combination of forcings. (a)-(d), 2-signal and (e), 3-signal detection and attribution analysis. (a), anthropogenic (ANT) and natural (NAT) forcing, (b), anthropogenic aerosol (AA) and natural (NAT) forcing, (c), anthropogenic aerosol (AA) and greenhouse gas (GHG) forcing, (d), greenhouse gas (GHG) and natural (NAT) forcing and (e), greenhouse gas (GHG), natural (NAT) and anthropogenic aerosol (AA) forcing. Results are shown for four observational datasets, CRU (CRU), Zhang (ZHA), VasClimO (VAS) and GPCC (GPCC). Crosses show the best-guess scaling factor for the multi-model mean, thick lines are the 90% confidence interval based on the raw variance and thin lines are the 90% confidence intervals when model variance has been doubled. The residual consistency test is passed for all cases. Stars (*) show where forcing is detected and two stars show where forcing is detected but inconsistent with a scaling factor of 1.

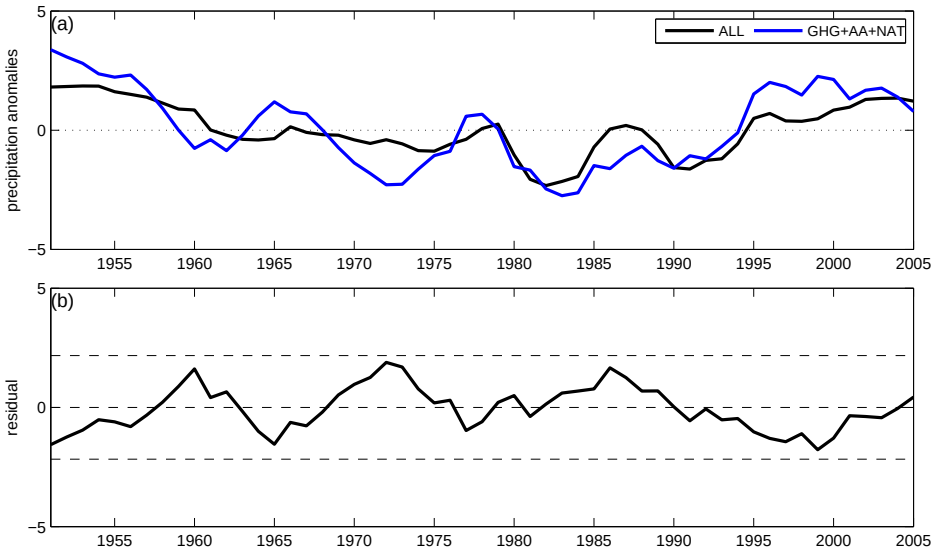


FIG. S13. Test of linearity assumption (a), The ALL multi-model mean and the sum of GHG+NAT+AA multi-model means for the NHSM region. (b), Residual (ALL multi-model mean minus the summed GHG+NAT+AA multi-model means). Dashed lines show 2 standard deviations of the internal variability from noise sample ensemble derived from the ALL forcing ensemble.

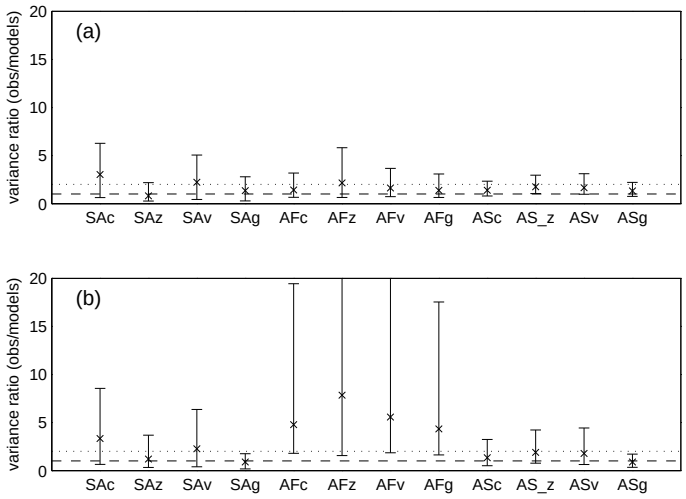


FIG. S14. Comparison of observed and modelled variance. Ratio of observed and ALL forced model simulations mean MJJAS precipitation variance for each region, SA is South America, AF is Africa and AS is Asia) and each observational datasets (c is CRU, z is Zhang v is VasClimO and g is GPCC). (a) unsmoothed, (b) 9-year running mean. The crosses show the median value and the bars are the 90% confidence interval. Dashed lines shows ratio of 1 and dotted line shows ratio of 2.